energies

MDPI

Article

Energy Balance and Local Unsteady Loss Analysis of Flows in a Low Specific Speed Model Pump-Turbine in the Positive Slope Region on the Pump Performance Curve

Guocheng Lu [1], Zhigang Zuo [1,*], Demin Liu [2] and Shuhong Liu [1,*]

[1] State Key Laboratory of Hydro Science and Engineering, Department of Energy and Power Engineering, Tsinghua University, Beijing 100084, China; lugc13@mails.tsinghua.edu.cn

[2] Research & Test Center, Dongfang Electric Machinery Co. Ltd, Deyang 618000, China; liudemin@dongfang.com

* Correspondence: zhigang200@tsinghua.edu.cn (Z.Z.); liushuhong@mail.tsinghua.edu.cn (S.L.)

Received: 26 April 2019; Accepted: 10 May 2019; Published: 14 May 2019

Abstract: The positive slope on the pump performance curve of pump-turbines suggests potential operational instabilities in pump mode. Previous research has indicated that the increase of the hydraulic loss caused by sudden changes of flow patterns in pump-turbines is responsible for the positive slope, however its detailed flow mechanism is still unclear. A low specific speed model pump-turbine was numerically investigated against experiments in the present study, by applying unsteady RANS (Reynolds-Averaged Navier–Stokes equations) simulations with a v^2-f turbulence model. The mechanism of occurrence of the positive slope on the pump performance curve was discussed regarding the energy balance, as this region appears when the value of $\frac{\partial P_u}{\partial Q}$ is larger than the critical value $\frac{P_u}{Q}$. An unsteady local loss analysis, derived from the energy equation, was conducted to illustrate the contribution of local flow patterns to the loss in corresponding hydraulic components. The variation of the kinetic energy of the mean flow was taken into account for the first time so that this method can be applied to highly time dependent flow patterns, e.g., a rotating stall in the present study. The investigations on the flow patterns revealed that some guide vane channels stalled with a larger discharge coefficient than the positive slope region. Several guide vane channels near the stalled channels were stalling with minor decrease of the discharge coefficient, leading to sudden increases of the input power and the loss. When the discharge coefficient slightly decreased in further, the pump-turbine operated into the positive slope region, and the rotating stall with 3 stall cells appeared, proven by the FFT (Fast Fourier Transform) and cross-phase analysis on the pressure fluctuations.

Keywords: pump-turbine; positive slope; instability; energy balance; unsteady loss analysis

1. Introduction

Pumped hydroelectric storage (PHS) is widely established for utility-scale electricity storage, utilizing relatively cheap electricity from the power grid during off-peak hours to move water from a lower reservoir to an upper one to store energy, and releasing the water from the upper reservoir to generate power at a higher price during periods of high electricity demand. This technology has been developed rapidly in the past several decades, to compensate the increasing application of the renewable energy, for its benefits of load-levelling, grid frequency regulation, and spinning reserves [1].

The earliest designs of PHS used separate pump and turbine units. Since the 1950s, the utilization of single reversible pump-turbines has become the dominant design for PHS, among which the Francis

pump-turbine (referred to pump-turbine hereinafter) prevails. Four major hydraulic components are included in the pump-turbine [2]: (1) Draft tube, serves as the inlet pipe in pump mode, and the diffused outlet pipe in turbine mode; (2) Impeller, transfers energy between the motor/generator and water; (3) Stator, guides the flow into/out of the impeller; (4) Spiral casing, generates a circumferentially uniform flow into/out of the stator. The specific speed ($n_q = \frac{n\sqrt{Q}}{H^{0.75}}$, where n, Q and H represent the rotating speed, the flow rate and the head respectively) is the key parameter to determine the appropriate impeller type and shape for given nominal conditions. For pump-turbines, impellers with a low specific speed correspond to high head or low flow rate, characterized by a narrow and long impeller channel. In recent years, higher head and larger unit capacity are being adopted to reduce manufacturing and construction costs, as well as to increase the unit hydraulic efficiencies [3], suggesting an increasing demand for the application of low specific speed pump-turbines.

Since pump-turbines frequently switch among diverse working conditions, operational instabilities leading to startup or shutdown failures are crucial issues to the application of pump-turbines [4]. The positive slope on the pump performance curve of the pump-turbine is often regarded as an 'unstable' performance characteristic causing potential startup failures in pump mode, accompanied with severe noise and vibration [2]. For low specific speed pump-turbines with high head, the possible damage caused by the positive slope is heavier due to the larger amplitudes of pressure fluctuations. The criterion of occurrence of this instability can be clarified through small perturbation analysis, illustrated in details as follows:

The hydraulic energy balance is applied to the control volume V containing the pump-turbine (in pump mode), the upper and lower reservoirs and all the pipes (Figure 1) to obtain the equation governing the system's behavior as shown [1]:

$$g\Delta z + gH_{loss} + \frac{1}{Q}\int_V \frac{\partial}{\partial t}\left(\frac{U^2}{2}\right)dV = gH \tag{1}$$

where H, H_{loss}, Δz, U, g, and Q represent the head of the pump-turbine, the head loss in pipes, the altitude difference between the upper and lower reservoirs, the velocity in the pipe, the gravitational acceleration and the flow rate respectively. The head loss is expressed with the flow rate Q, a loss coefficient K_s and a reference section area A:

$$gH_{loss} = \frac{1}{2}K_s U^2 = K_s\frac{Q^2}{2A^2} \tag{2}$$

A hydraulic inductance L_h is introduced to express the inertia term in Equation (1):

$$\frac{1}{Q}\int_V \frac{\partial}{\partial t}\left(\frac{U^2}{2}\right)dV = \frac{1}{A}\frac{\partial Q}{\partial t} = L_h\frac{\partial Q}{\partial t} \tag{3}$$

Therefore, the governing equation is simplified as

$$g\Delta z + K_s\frac{Q^2}{2A^2} + L_h\frac{\partial Q}{\partial t} = gH \tag{4}$$

Small perturbations of the flow rate (δQ) and the head (δH) have been introduced into Equation (4) to study the instability of the system, and Equation (4) becomes:

$$g\Delta z + K_s\frac{(Q+\delta Q)^2}{2A^2} + L_h\frac{\partial (Q+\delta Q)}{\partial t} = g(H+\delta H) \tag{5}$$

Then the governing equation to the system can be obtained by ignoring the higher order terms from (Equation (4) to Equation (5)), as follows:

$$L_h \delta \dot{Q} + K_s \frac{Q}{A^2} \delta Q = g \delta H = g \frac{\partial H}{\partial Q} \delta Q \tag{6}$$

Equation (6) can be written as:

$$L_h \delta \dot{Q} + \left(K_s \frac{Q}{A^2} - g \frac{\partial H}{\partial Q} \right) \delta Q = 0 \tag{7}$$

Since $L_h > 0$, the stability condition derived from the governing equation implies:

$$K_s \frac{Q}{A^2} > g \frac{\partial H}{\partial Q} \tag{8}$$

Since the value of $K_s \frac{Q}{A^2}$ is always positive, the occurrence of positive slopes on pump performance curves is an insufficient but necessary condition of instability.

While positive slopes on pump performance curves are often detected in pump-turbines, the theoretical pump performance curve should be monotonically decreasing according to the conservation of angular momentum with the blade-congruent flow assumption, i.e., an infinite number of congruent blades without thickness, hence all the fluid flows along the blade. The measured head is less than the theoretical head due to a number of factors, e.g., the viscosity of fluid, turbulence, and the vortex. The difference between them is defined as "hydraulic loss". The positive slope is often detected in fact due to a sudden increase of hydraulic loss in partload condition [5], as shown in Figure 2. The flow mechanisms of this phenomenon in a pumping system, including the pump-turbine, are extraordinary complex. Gülich [5] summarized them as a "sudden change" of flow patterns at the entrance or exit of the impeller, leading to the sudden increase of the hydraulic loss. In pump-turbines diverse flow pattern changes, including rotating stall [6,7], flow separation shift [8,9] and pre-rotation of inflow [6], have been reported when operating in the positive slope region. Thus, the flow pattern in the pump-turbine working in this region may be highly turbulent, unsteady and swirling.

Although various experimental studies including PIV (Particle Image Velocimetry) measurements [10], and bubble injections [11] were conducted for the purpose of studying the flow patterns in the pump-turbine, the descriptions of these flow patterns were still limited. Numerical simulation is thereby a major tool, which is less expensive, more flexible and leads to a more detailed database of the flow field. Unsteady simulation is necessary to predict flow patterns in the pump-turbine operating in the positive slope region, considering that these flow patterns are highly time-dependent (e.g., rotating stall). While LES (Large Eddy Simulation) is better to predict the flow field in theory, the corresponding requirements on the spatial discretization are too high to be acceptable in most engineering cases [7]. Hence RANS (Reynold Averaged Navier-Stokes) simulations with linear turbulence models were widely applied to study the flows in pump-turbines [12–14]. The results proved its capability to predict the performances, pressure fluctuations and flow patterns at design conditions, while the precision at off-design conditions still need improvement. The possible explanations for this inaccuracy of simulation at off-design conditions may lie in the unsteadiness and turbulent flow structures, which may be damped out in the RANS simulations with linear turbulence models [15–17]. In order to avoid this disadvantage, some research applied v^2-f, a non-linear turbulence model, to simulate the flow field in the pump-turbine at pump mode [12,13]. Not only the performance, the pressure fluctuations and the flow patterns were also well predicted.

As discussed above, the hydraulic loss represents the difference between the measured head and the theoretical head, indicating the difference between the real flow and the ideal flow with the blade-congruent flow assumption. Although it is generally accepted that the sudden change of flow patterns leading to a sharp increase of the hydraulic loss is responsible to the positive slope [1],

its detailed flow mechanism is still unclear, since it is difficult to quantitatively measure the difference described above, and to discuss the relationship between this difference and the hydraulic loss. Instead, it is easier to discuss the relationship between the flow patterns and the energy through the energy equation. For the purpose of a better understanding of the flow phenomena related to the positive slope, unsteady RANS simulations with v^2-f turbulence model were conducted to adequately predict the flow patterns in a low-specific speed pump-turbine operating at partload conditions, near the positive slope region. The energy balance analysis was applied to discuss the mechanism of the occurrence of the positive slope. The unsteady local loss analysis based on the energy equation was also conducted to study the contribution of local flow to the loss.

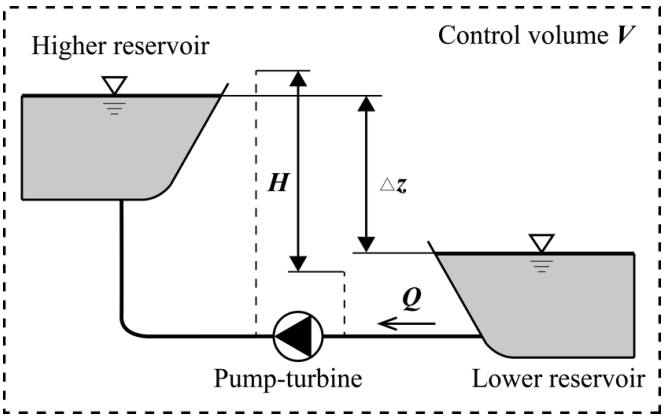

Figure 1. Pump-turbine system in pump mode.

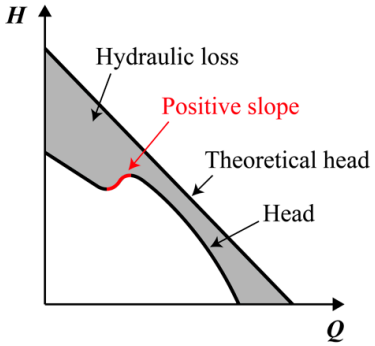

Figure 2. Positive slope in pump performance curve.

2. Methodology

In the present study, a low specific speed ($n_q = \frac{n\sqrt{Q}}{H^{0.75}} = 27$, where n, Q represent the rotating speed and the flow rate respectively) model pump-turbine was investigated. The geometric parameters of the pump-turbine are listed in Table 1. The pump performance curves of this pump-turbine at various guide vane openings (GVO) were experimentally examined on the *DF150 Hydraulic Test Rig* of Dongfang Electric Corporation (DEC), China. The details of the related experiments were stated in Ref [18]. The geometric parameters used in the numerical simulations described in the next Sections are selected according to the experimental parameters. Figure 3 demonstrates the experimental results of pump performance curves, where the relative GVO α is defined as the ratio of the individual GVO over the optimum GVO (18). $\varphi = \frac{Q}{nD^3}$ and $\psi = \frac{gH}{n^2D^2}$ represent the discharge coefficient and the energy coefficient respectively, where n and D respectively represent the rotational speed and the diameter of the impeller. Detailed examination of each curve shows that the positive slope region exists for each GVO curve except at the optimum GVO.

Table 1. Geometric parameters of the model pump-turbine.

Parameter	Value
Number of blades	7
Impeller inlet diameter (mm)	250
Impeller outlet diameter (mm)	550
Number of guide vanes	20
Height of guide vanes (mm)	37.75

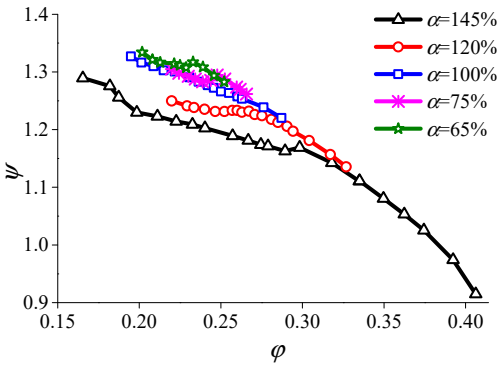

Figure 3. Experimental pump performance curves at various guide vane openings (GVOs).

The computational domain of the pump-turbine built for numerical simulations is shown in Figure 4, including its major hydraulic components, i.e., the draft tube, the impeller, the guide vanes and stay vanes, and the spiral casing. Velocity flow inlet and static pressure outlet were chosen as the boundary conditions.

Unsteady numerical simulations based on RANS method were applied in the present study. The time taken by the impeller to rotate 2 was determined as the computational time step size. The Courant number is less than 1, leading to convergent simulations. The calculation load is also acceptable at the same time. The mesh in the impeller was set as "grid motion" with impeller rotational speed (1100 r/min), and "no-slip" conditions were imposed on all stationary walls. The "sliding interface" was set between the rotating and stationary components to transmit the data. For the purpose of measuring the pressure fluctuations, static pressure monitoring points were positioned near the upper wall of the draft tube, the vaneless space (the gap between the impeller and the guide vane), the guide vane and the stay vanes channels in the simulation (Figure 5). The pressure fluctuations at the locations marked in Figure 5 were also measured in the experiments. In addition, the middle spanwise hub-to-shroud surface and the guide vane symmetry plane were set in the pump-turbine to discuss the flow patterns in the impeller and the guide vane channels, respectively (Figure 6).

A non-linear turbulence mode, i.e., v2-f turbulence model, is applied in the present study, in which no wall function is utilized. In this turbulence model, two more equations, namely the transport equation for $\overline{v^2}$, $\frac{\partial}{\partial t}\left(\rho\overline{v^2}\right)+\frac{\partial}{\partial x_i}\left(\rho\overline{v^2}u_i\right)=\rho kf-6\rho\overline{v^2}\frac{\varepsilon}{k}+\frac{\partial}{\partial x_j}\left[\left(\mu+\frac{\mu_t}{\sigma_\varepsilon}\right)\frac{\partial\overline{v^2}}{\partial x_j}\right]+S_{\overline{v^2}}$, and the elliptic equation for the relaxation function f, $f-L^2\frac{\partial^2 f}{\partial x_j^2}=(C_1-1)\frac{\frac{2}{3}-\frac{\overline{v^2}}{k}}{T}+C_2\frac{P}{\rho k}+\frac{5\frac{\overline{v^2}}{k}}{T}+S_f$, are solved in addition to k equation, $\frac{\partial}{\partial t}(\rho k)+\frac{\partial}{\partial x_i}(\rho k u_i)=P-\rho\varepsilon+\frac{\partial}{\partial x_j}\left[\left(\mu+\frac{\mu_t}{\sigma_k}\right)\frac{\partial k}{\partial x_j}\right]+S_k$, and ε equation, $\frac{\partial}{\partial t}(\rho\varepsilon)+\frac{\partial}{\partial x_i}(\rho\varepsilon u_i)=\frac{C'_{\varepsilon1}P-C'_{\varepsilon2}\rho\varepsilon}{T}+\frac{\partial}{\partial x_j}\left[\left(\mu+\frac{\mu_t}{\sigma_\varepsilon}\right)\frac{\partial\varepsilon}{\partial x_j}\right]+S_\varepsilon$, where the turbulence time and length scales are respectively defined as $T'=\max\left(\frac{k}{\varepsilon},6\sqrt{\frac{v}{\varepsilon}}\right)$, $T=\min\left(T',\frac{\alpha}{\sqrt{3}}\frac{k}{\overline{v^2}C_u\sqrt{2S^2}}\right)$, $L'=\min\left(\frac{k^{3/2}}{\varepsilon},\frac{1}{\sqrt{3}}\frac{k^{3/2}}{\overline{v^2}C_u\sqrt{2S^2}}\right)$, and $L=C_L\max\left(L',C_\eta\left(\frac{v^3}{\varepsilon}\right)^{1/4}\right)$ [19,20]. The turbulence viscosity is defined as $\mu_t=\rho C_u\overline{v^2}T$. The coefficients are respectively selected as $\alpha=0.6$, $C_1=1.4$, $C_2=0.3$, $C_{\varepsilon1}=1.4$, $C_{\varepsilon2}=1.9$, $C_\eta=70$, $C_\mu=0.22$, $C_L=0.23$, $\sigma_k=1$, $\sigma_\varepsilon=1.3$, and $C'_{\varepsilon1}=C_{\varepsilon1}\left(1+0.045\sqrt{k/\overline{v^2}}\right)$.

Although this model was originally developed for attached or mildly separated boundary layers, it could also accurately simulate flows dominated by separation [19,20]. Semi-Implicit Method for Pressure-Linked Equations Consistent (SIMPLEC) algorithm with a second-order spatial discretization and a first-order implicit transient formulation was chosen as the pressure–velocity coupling method, which is widely applied in the simulations of flows in pump-turbines.

A structured computational grid system for the whole hydrodynamic domain was developed in the commercial software the Integrated Computer Engineering and Manufacturing code for Computational Fluid Dynamics (ICEM-CFD). Local grid refinements to the boundary layers were applied in the impeller, guide vane and stay vane regions to achieve $y^+ \approx 1$ for the first grid layer, considering that no wall function is utilized.

To determine the number of the grids for the whole computational domain, three grid systems with different number of grids were respectively built. Then η_h (the hydraulic efficiency) and ψ at the Best Efficiency Point (BEP) of the optimum GVO in the three grid systems were computed, as listed in Table 2. The relative variation of both η_h and ψ is larger than 5% when the number of the grid increased from grid system 1 to 2, while it is smaller from 2 to 3. Therefore, the grid system 3 with 17,000,000 number of grid is acceptable for the investigations in the present study.

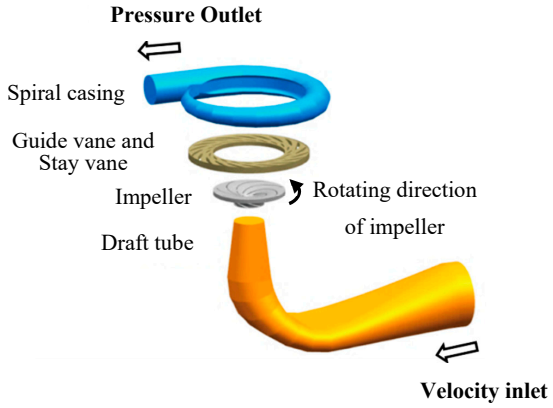

Figure 4. Computational Fluid Dynamics (CFD) computational domain (pump mode).

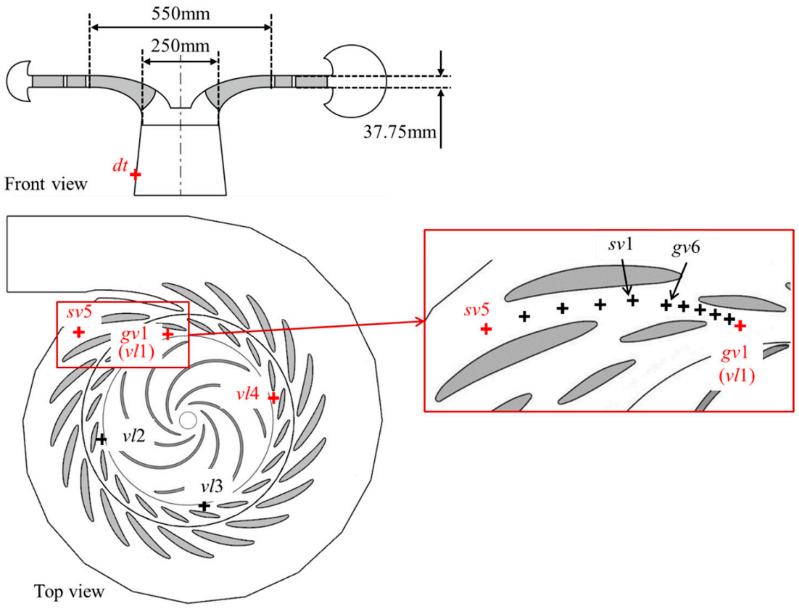

Figure 5. Static pressure monitoring points in the draft tube, the vaneless space, guide vane, and stay vane channels.

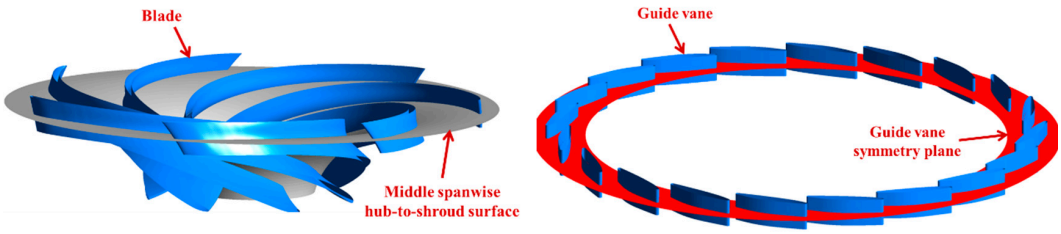

Figure 6. Planes for data analysis (**a**) The middle spanwise hub-to-shroud surface and (**b**) the guide vane symmetry plane.

Table 2. η_h and H at BEP of the optimum GVO in the three grid systems.

	Number of Grids	η_h (%)	ψ
Grid system 1	8,000,000	86.5	1.08
Grid system 2	12,000,000	91.1	1.17
Grid system 3	17,000,000	91.3	1.17

3. Results and Discussions

3.1. Validation of the Simulations

The pump performance curves of the pump-turbine at three various GVOs (α = 45%, 75% and 145%) are well predicted, as shown in Figure 7, including the occurrence of the positive slope at all GVOs. The calculated fluctuations of the pressure coefficient ($C_p = \frac{p}{\frac{1}{2}\rho {u_2}^2}$,where u_2 represents the relative velocity at impeller exit) at vaneless space ($gv1$), and the FFT (Fast Fourier Transform) results at working conditions I (φ = 0.294) and II (φ = 0.227) are illustrated in Figures 8 and 9, respectively. Pressure fluctuation frequencies were normalized against the rotational frequency f_n. It can be seen that the pressure fluctuations at the blade passing frequency (BPF) and its harmonic were well predicted in the simulations. In addition, a pressure fluctuation component with a low frequency was detected in both experiments (8% f_n = 1.46 Hz) and simulations (9% f_n = 1.65 Hz) at condition II.

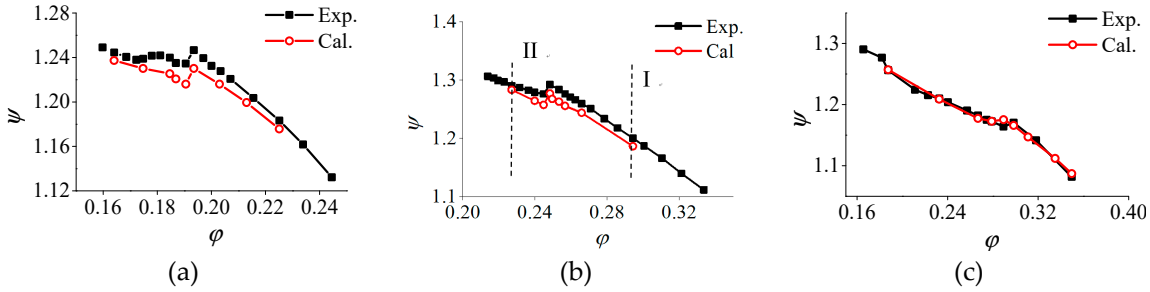

Figure 7. Pump performance curves at (**a**) α = 45%, (**b**) α = 75% and (**c**) α = 145%.

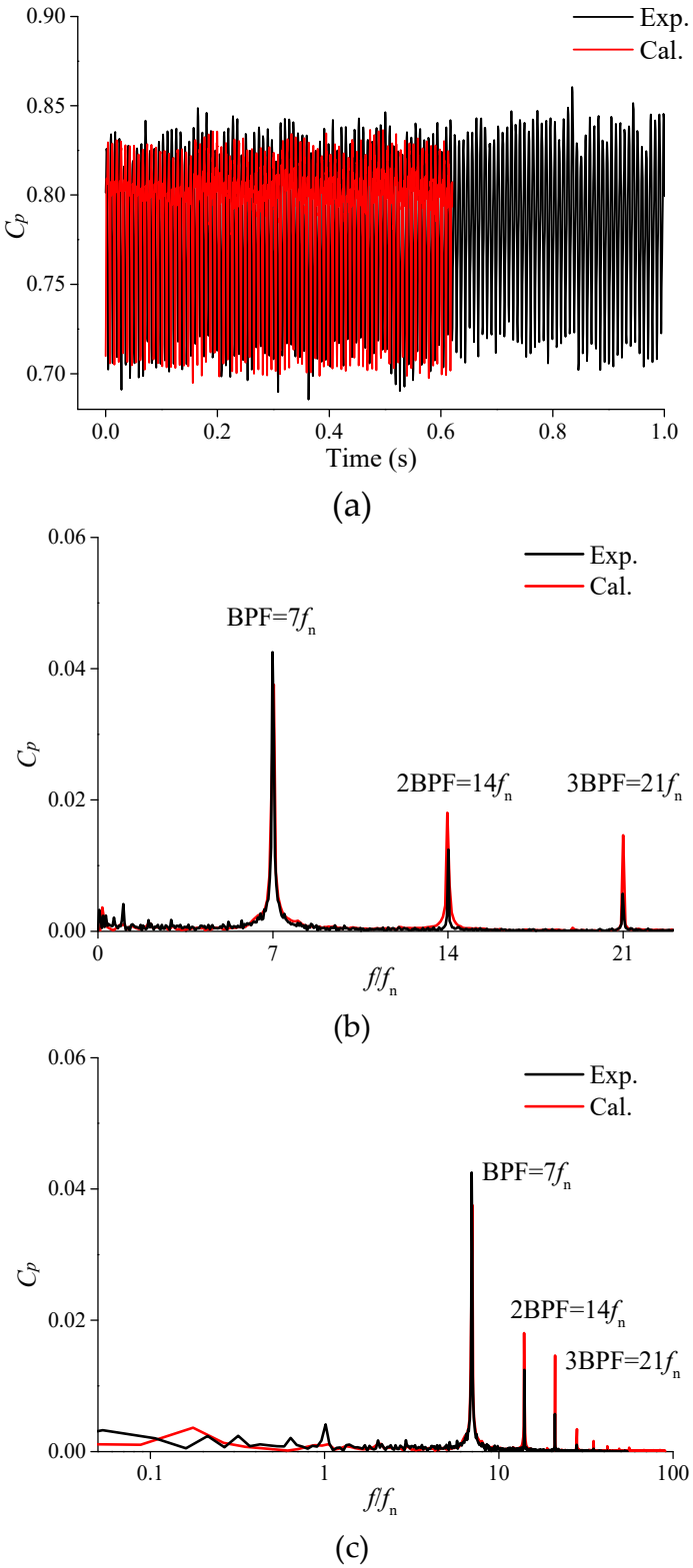

Figure 8. Pressure signals at vaneless space (*gv*1) at condition I. (**a**) Pressure fluctuations, and FFT (Fast Fourier Transform) results with (**b**) linear and (**c**) logarithmic abscissa.

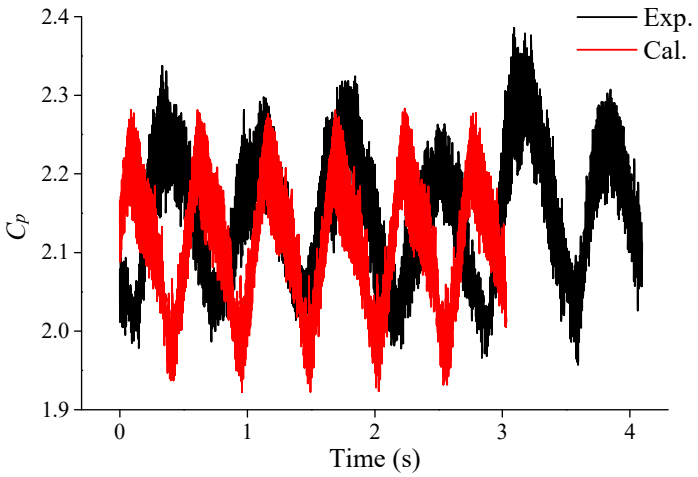

(a)

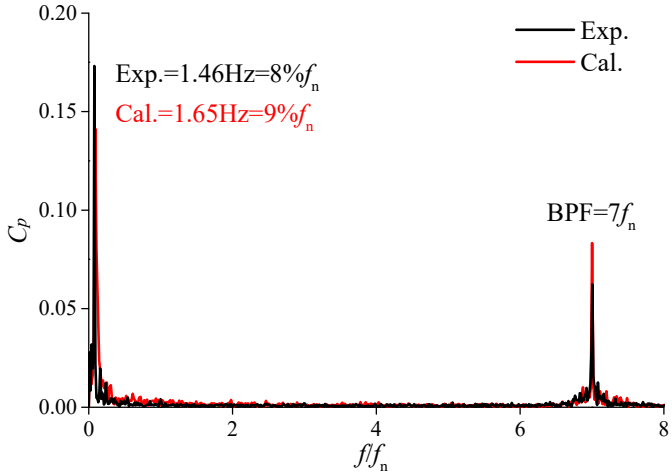

(b)

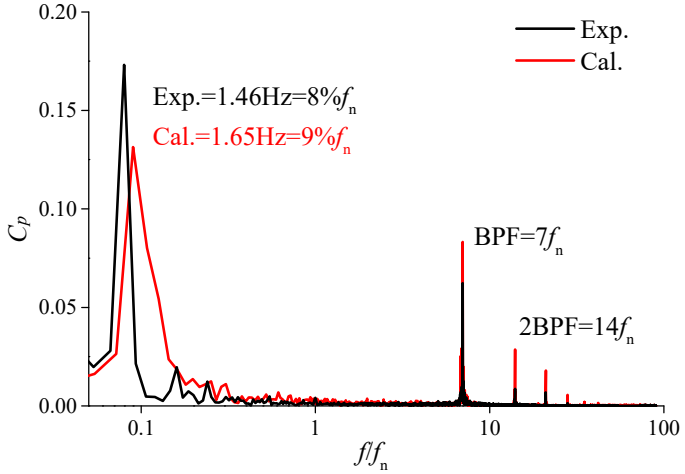

(c)

Figure 9. Pressure signals at vaneless space (gv1) at condition II. (**a**) Pressure fluctuations, and FFT results with (**b**) linear and (**c**) logarithmic abscissa.

3.2. Pump Performance and Head Loss

The pump performance curve and head loss coefficient ($\psi_L = \frac{gH_L}{n^2D^2}$, where $H_L = H_{inlet} - H_{outlet}$ is the head loss in the corresponding hydraulic component. H_{inlet} and H_{outlet} are the head at the inlet and the outlet of this component, respectively) at α = 75% are illustrated in Figure 10. Three working conditions near the positive slope are defined as III, IV, and V from large to small discharge coefficient. It should be mentioned that condition V is the left bound of the positive slope region. The head loss coefficient in the impeller and guide vane channels are larger than in the other hydraulic components for all conditions. The total head loss coefficient increases gradually with decreasing discharge coefficient, while a sudden increase is detected when the discharge coefficient decreases from III to IV.

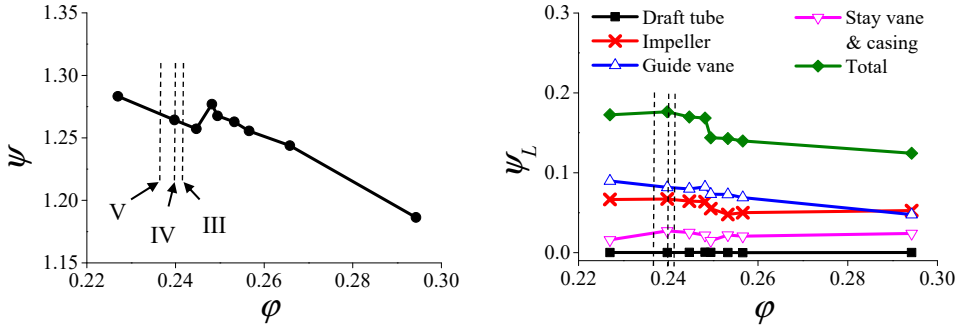

Figure 10. Performance and loss analysis. (**a**) Pump performance curve and (**b**) head loss coefficient in each component.

3.3. Pressure Fluctuations

3.3.1. Conditions III and IV

The FFT results of the pressure coefficient at conditions III and IV (out of the positive slope region) are shown in Figure 11. The dominant frequency of the fluctuations is the blade passing frequency ($f_1 = 7f_n$ = 128 Hz). The amplitude of this fluctuation component is strongest near the entrance of the guide vane channel, matching the conclusion in the previous study [21,22].

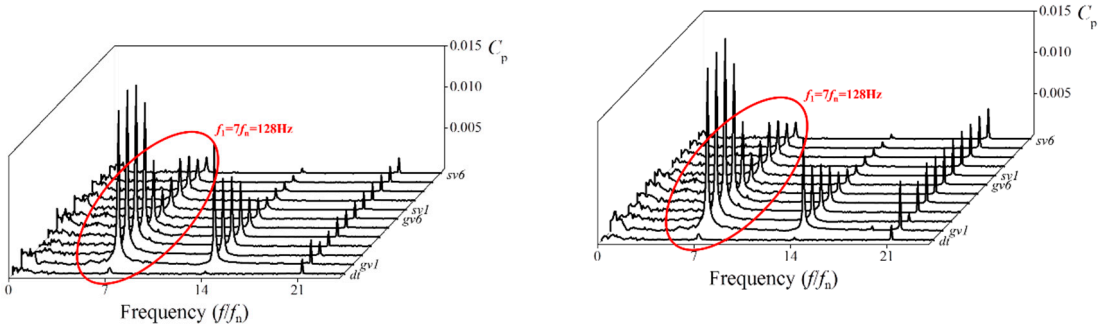

Figure 11. FFT results of pressure fluctuations at condition (**a**) III and (**b**) IV.

3.3.2. Condition V

The FFT results of pressure coefficient at condition V are shown in Figure 12. A low-frequency pressure fluctuation signal ($f_2 = 9\% f_n$ = 1.65 Hz) is detected and becomes the dominant frequency fluctuation, instead of the fluctuation at blade passing frequency. This low-frequency fluctuation,

which is stronger at the vaneless space than that at other locations, may be caused by the rotating stall according to previous studies [1,13].

In the case of rotating stalls, the number of the stall cells could be determined with the analysis on the cross-phase delay of monitoring points at deferent circumferential positions, according to:

$$N = \frac{\theta_{RS}}{\theta} \tag{9}$$

where N is the number of the stall cells. θ represents the separation angle between two monitoring points at deferent circumferential positions, while θ_{RS} represents the cross-phase delay of the low-frequency fluctuation caused by the rotating stall between the two points. The cross-phase delays of the low-frequency fluctuation (1.65 Hz) between several couples of monitoring points were illustrated in Table 3. It could be concluded that three rotating cells exist since the separation angles of the three couples of monitoring points are 90, while the cross-phase delays are about 270 = 90 × 3. The cross-phase delays of the three couples of points vary slightly, suggesting that the rotational speed of stall cells is not constant at different circumferential positions.

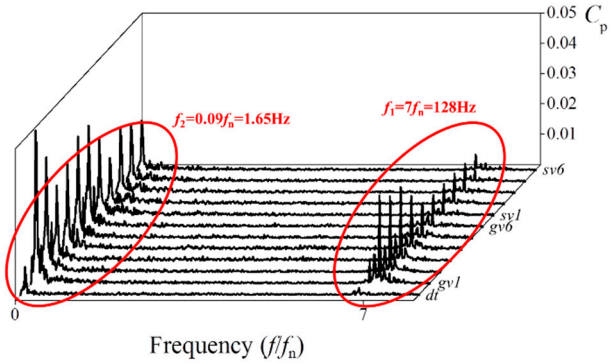

Figure 12. FFT results of pressure fluctuations at condition V.

Table 3. Cross-phase delays between several couples of monitoring points at condition V.

Couple of Monitoring Points	*vl*1-*vl*2	*vl*2-*vl*3	*vl*3-*vl*4	*vl*4-*vl*1
Cross-phase delay of 1.65 Hz	272.8	260.8	304.6	241.8

3.4. Energy Balance Analysis

The mechanical energy transfers to the fluid in pump-turbines through the rotation of the impeller. Part of it becomes the mechanical energy of the fluid, while the rest is converted to the internal energy and turbulent kinetic energy due to the viscosity and turbulence. The mechanical power transferred to the fluid through the impeller is defined as the input power $P_{in} = M_z\omega$, where M_z is the axial moment acting on the impeller and ω is the rotational speed of the impeller. The mechanical power obtained by the fluid is defined as the useful power $P_u = \rho gHQ$. To satisfy the energy balance, the difference of P_{in} and P_u is defined as the loss $P_L = P_{in} - P_u$.

The head H can be regarded as a function of the flow rate Q and it can be derived from the definition of the useful power that:

$$\frac{\partial P_u}{\partial Q} - \rho gH = \frac{\partial P_u}{\partial Q} - \frac{P_u}{Q} = \rho g \frac{\partial H}{\partial Q} Q \tag{10}$$

Regarding $Q > 0$, it can be concluded that the necessary and sufficient condition of the occurrence of the positive slope is that the value of $\frac{\partial P_u}{\partial Q}$ is larger than the critical value $\frac{P_u}{Q}$. When reducing the flow rate, the decrease of the input power and the increase of the torque can result in the decrease of the useful power, which may lead to the positive slope in the pump performance curve.

For the simulating results in the present study, the input power coefficient ($\lambda = \frac{P_{in}}{n^3 D^5}$), the useful power coefficient ($\lambda_u = \frac{P_u}{n^3 D^5}$,) and the loss coefficient in each hydraulic component ($\lambda_L = \frac{P_L}{n^3 D^5}$) are shown in Figure 13. λ_{in} and λ_u increase gradually with increasing discharge coefficient, with an exception of λ_{in} at the condition III to IV. A sudden decrease of λ_L at condition III to IV was also detected. λ_L in the impeller and the guide vane channels are larger than that in the other hydraulic components.

The values of $\frac{\partial \lambda_u}{\partial \varphi}$ and $\frac{\lambda_u}{\varphi}$ at each condition are calculated as shown in Figure 14, to validate the theoretical conclusion of stability criterion above. Since only finite number of conditions can be calculated in the simulations, the value of $\frac{\partial \lambda_u}{\partial \varphi}$ was computed according to the following equation:

$$\left(\frac{\partial \lambda_u}{\partial \varphi}\right)_i = \frac{\lambda_{u,i+1} - \lambda_{u,i}}{\varphi_{i+1} - \varphi_i} \tag{11}$$

where the subscript i indicates the ith condition, while i+1 means the condition next to i with a larger discharge coefficient. Only at condition V, where the positive slope on pump performance curve was detected, $\frac{\partial \lambda_u}{\partial \varphi}$ is larger than $\frac{\lambda_u}{\varphi}$, indicating that the value of $\frac{\partial P_u}{\partial Q}$ is larger than the critical value $\frac{P_u}{Q}$. This result fits with the theoretical conclusion, suggesting that the substantial decrease of λ_u from condition IV to V results in the positive slope in the pump performance curve. A further investigation shows that for the decrease of λ_u from condition IV to V, about 80% is attributed to the decrease of the input power coefficient while the remaining 20% is caused by the increase of the loss coefficient.

For a further understanding of the sudden variation of P_u, the mechanism of the decrease of the input power and the increase of the loss are discussed in Sections 4 and 5 respectively.

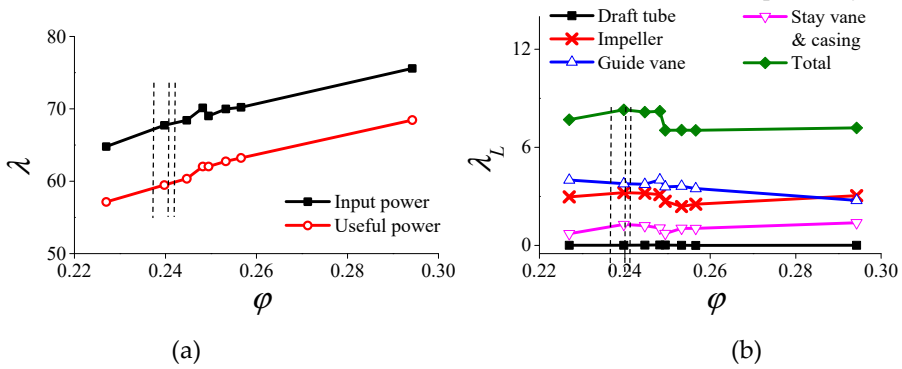

Figure 13. Performance and loss analysis. (**a**) Input power coefficients and useful power coefficient as well as (**b**) the loss coefficient in each component.

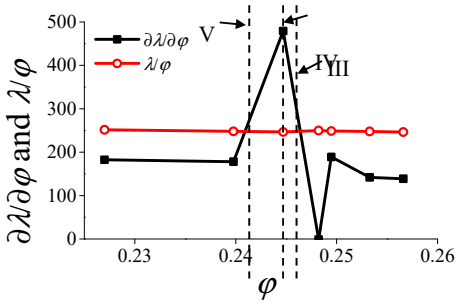

Figure 14. $\frac{\partial \lambda_u}{\partial \varphi}$ and $\frac{\lambda_u}{\varphi}$ in every condition.

4. Analysis of the Input Power

The input power P_{in} is equal to the product of the axial moment acting on the impeller M_z and the rotational speed ω. Since the pump-turbine is operating at a constant rotational speed in the present study, the increase of the input power indicates the increase of the axial moment, which is generated by

the pressure and shear force distributed on the impeller. The two effects of pressure and shear force on the moment on the impeller were calculated, respectively. The pressure effect contributes over 98% to the moment. Therefore, the pressure distribution on the impeller was analyzed to explain the sudden increase of the input power coefficient from condition III to IV.

Figure 15 shows the intersections of every blade and the middle spanwise hub-to-shroud surface. The lines on the pressure sides and the suction sides of blades are respectively marked. Then the time-averaged pressure distributions on the lines on the both sides were respectively averaged, and compared between conditions III and IV. The increase of the pressure on the pressure side near the exit of the impeller from condition III to IV leads to the variation of M_z. This is responsible for the sudden change of the input power.

For a further understanding of this variation, the instantaneous pressure distributions on the pressure side of the impeller for both conditions are shown in Figure 16. It could be concluded that the region with high pressure near the exit of the impeller extended to the neighbor blade from condition III to IV, resulting in the increase of blade loading on the pressure side near the exit of the impeller. The instantaneous streamlines in the guide vane channels and pressure distributions on the pressure side of impeller are shown in Figure 17. It could be concluded that the stalled guide vane channels are responsible for the high-pressure regions on the blade. Several guide vane channels are stalling from condition III to IV, leading to the extension of the high-pressure region on the impeller.

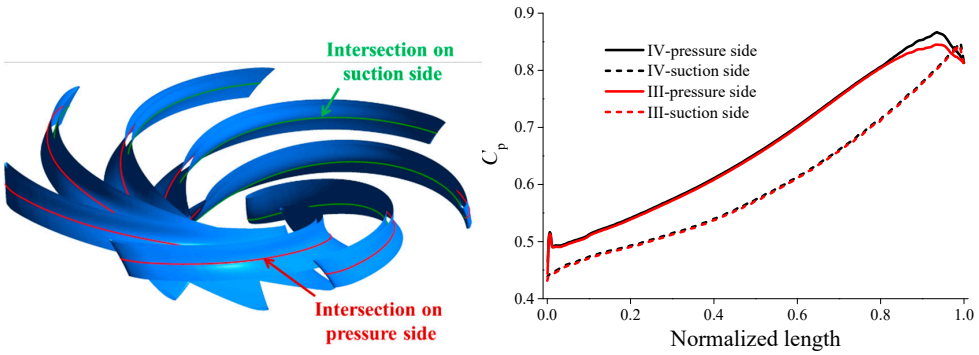

(a) (b)

Figure 15. Pressure distribution. (**a**) Intersections of blades and the middle spanwise hub-to-shroud surface and (**b**) time averaged pressure distribution at two conditions (locations of 0 and 1 represent the entrance and the exit of the impeller, respectively).

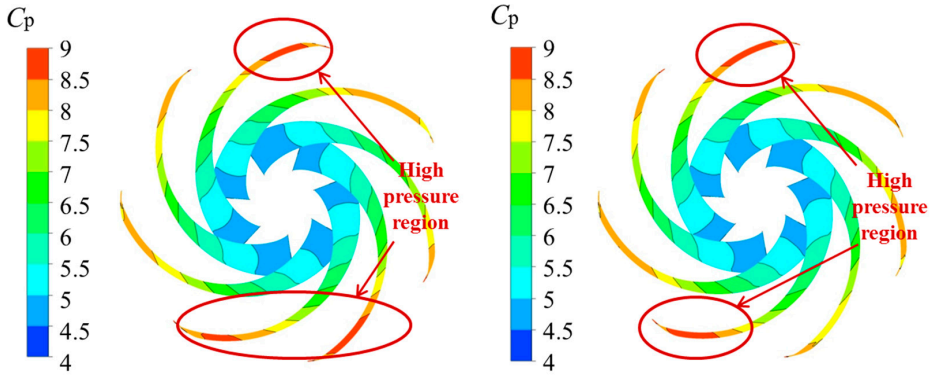

(a) (b)

Figure 16. Instantaneous pressure distributions on the pressure side of the impeller at condition (**a**) IV and (**b**) III.

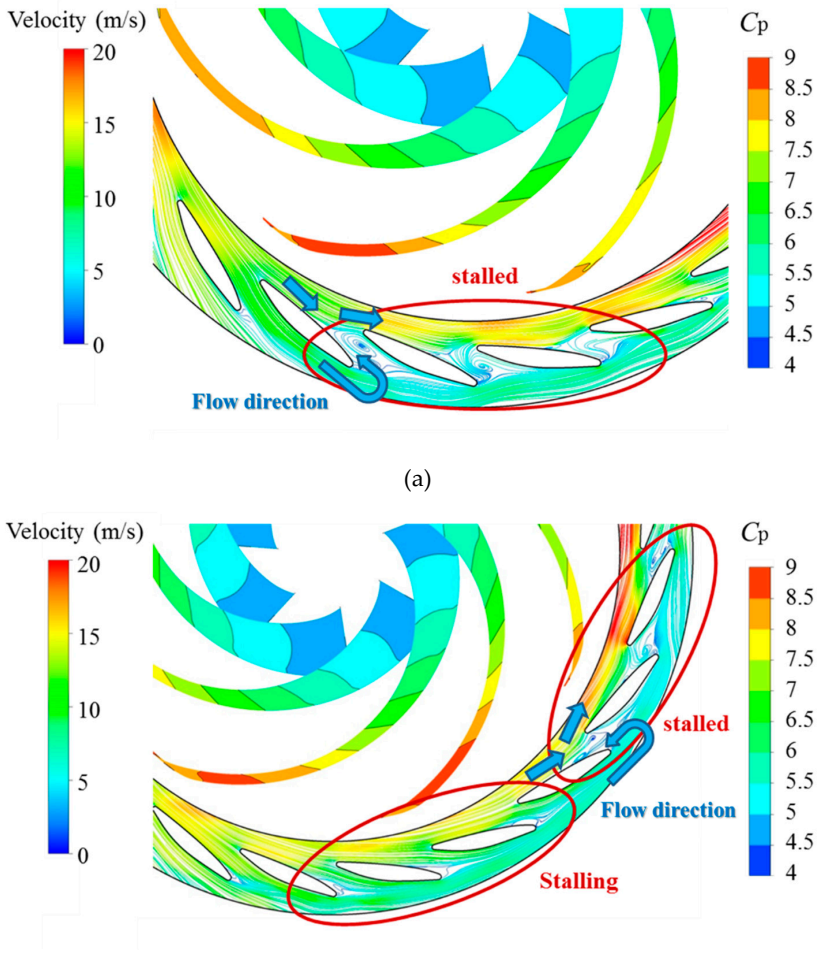

Figure 17. Instantaneous streamlines in the guide vane channels and pressure distributions on the pressure side of impeller at condition (**a**) IV and (**b**) III.

5. Analysis of the Loss

To better understand the relationship between the flow patterns and the loss in pump-turbines, a local loss analysis based on the energy equation was conducted at conditions III, IV, and V, to study the flow mechanism of the positive slope. Compared with previous studies [23–25], the variation of the kinetic energy of the mean flow is taken into account for the first time so that this local loss analysis could be applied to study the highly time dependent flow patterns. This is important for the discussion in the present study because of the existence of rotating stall, a typical highly time dependent flow pattern.

5.1. Local Loss Analysis Method

For an incompressible turbulent flow without heat transfer or temperature variation, the energy equation in stationary hydraulic components (including the draft tube, guide vane channels, stay vane channels and the spiral casing) can be simplified as follows:

$$\frac{\partial}{\partial t}\left(\frac{1}{2}\rho\overline{u}^2\right)+\frac{\partial\left[\overline{u}_j\left(\frac{1}{2}\rho\overline{u}^2+\overline{p}+\rho gz\right)\right]}{\partial x_j}=\frac{\partial(-\overline{u}_i\overline{\rho u_i'u_j'})}{\partial x_j}+\mu\frac{\partial(\overline{u}_i\overline{D_{ij}})}{\partial x_j}-(-\overline{\rho u_i'u_j'})\frac{\partial\overline{u}_i}{\partial x_j}-\mu\overline{D_{ij}}\frac{\partial\overline{u}_i}{\partial x_j} \quad (12)$$

where $D_{ij} = \frac{\partial u_i}{\partial x_j} + \frac{\partial u_j}{\partial x_i}$, μ represents the kinematic viscosity, $\overline{a}$ and a' are the time averaged value and the fluctuation of a physical quantity a, respectively.

Then each term in Equation (12) is integrated over the total volume V of a hydraulic component, and Equation (12) becomes:

$$\begin{aligned} P_u = &-\iiint_V \frac{\partial}{\partial t}\left(\frac{1}{2}\rho\overline{u}^2\right)dV + \iiint_V \frac{\partial(-\overline{u_i}\overline{\rho u_i' u_j'})}{\partial x_j}dV + \iiint_V \mu\frac{\partial(\overline{u_i}\overline{D_{ij}})}{\partial x_j}dV \\ &-\iiint_V (-\overline{\rho u_i' u_j'})\frac{\partial \overline{u_i}}{\partial x_j}dV - \iiint_V \mu\overline{D_{ij}}\frac{\partial \overline{u_i}}{\partial x_j}dV \end{aligned} \tag{13}$$

In order to analyze the flow in the impeller, the input power should be taken into account. A source term is added to the equation as follow:

$$\begin{aligned} P_u = &-\iiint_V \frac{\partial}{\partial t}\left(\frac{1}{2}\rho\overline{u}^2\right)dV + \iiint_V \frac{\partial(-\overline{u_i}\overline{\rho u_i' u_j'})}{\partial x_j}dV + \iiint_V \mu\frac{\partial(\overline{u_i}\overline{D_{ij}})}{\partial x_j}dV \\ &-\iiint_V (-\overline{\rho u_i' u_j'})\frac{\partial \overline{u_i}}{\partial x_j}dV - \iiint_V \mu\overline{D_{ij}}\frac{\partial \overline{u_i}}{\partial x_j}dV + P_{in} \end{aligned} \tag{14}$$

By comparing the definition of P_L and Equation (14), the loss in every hydraulic component can be expressed as follows:

$$\begin{aligned} P_u = &-\iiint_V \frac{\partial}{\partial t}\left(\frac{1}{2}\rho\overline{u}^2\right)dV + \iiint_V \frac{\partial(-\overline{u_i}\overline{\rho u_i' u_j'})}{\partial x_j}dV + \iiint_V \mu\frac{\partial(\overline{u_i}\overline{D_{ij}})}{\partial x_j}dV \\ &\text{Term 1} \qquad\qquad \text{Term 2} \qquad\qquad \text{Term 3} \\ &+\iiint_V (-\overline{\rho u_i' u_j'})\frac{\partial \overline{u_i}}{\partial x_j}dV + \iiint_V \mu\overline{D_{ij}}\frac{\partial \overline{u_i}}{\partial x_j}dV \\ &\text{Term 4} \qquad\qquad \text{Term 5} \end{aligned} \tag{15}$$

Thus, the loss in every hydraulic component is determined by five terms. Term 1 represents variation of the kinetic energy of the mean flow. Terms 2 and 3 correspond to the diffusion of the kinetic energy of the mean flow. Term 4 is the turbulent kinetic energy production, which is responsible for the transfer of the kinetic energy of the mean flow to the turbulent kinetic energy. Term 5 corresponds to the viscous dissipation.

Since RANS simulations were conducted in the present study, it should be noted that the Reynold stress $\rho\overline{u_i' u'}$ was calculated as follows:

$$\rho\overline{u_i' u_j'} = -\frac{1}{2}\mu_t\left(\frac{\partial \overline{u_i}}{\partial x_j} + \frac{\partial \overline{u_j}}{\partial x_i}\right) + \frac{2}{3}\rho k\delta_{ij} \tag{16}$$

where μ_t is the eddy viscosity, k represents the turbulent kinetic energy and δ_{ij} is Kronecker delta, being equal to 1 if $i = j$ and 0 otherwise.

5.2. Physical Phenomena Responsible for the Loss

According to the analysis in the previous discussion, the loss includes four parts: the variation of the kinetic energy of the mean flow (Term 1), the kinetic energy of the mean flow diffusion (Term 2 and 3), the turbulent kinetic energy production (Term 4), and the viscous dissipation (Term 5). Since the rotating stall is a highly time dependent flow pattern, and do not exist in conditions III and IV, it is not necessary to discuss the contribution of the variation of the kinetic energy of the mean flow at the two conditions. The contribution of each part to the loss will be investigated and the relationship with the flow patterns will be discussed.

5.2.1. Condition III and IV

Figure 18 illustrates the compositions of the loss coefficient at conditions III and IV. The draft tube is not taken into account, since the loss in that component is low compared to the others (shown in Figure 13). It could be concluded that the turbulent kinetic energy production is much larger than the other two terms, suggesting that most loss of the energy converts to the turbulent kinetic energy. This result is supported by the fact that the flow in pump-turbines is highly turbulent. Regarding the larger losses in the impeller and guide vane channels than in the other hydraulic components, the distributions of the turbulent kinetic energy production in these two components were specifically discussed.

The instantaneous distributions of the turbulent kinetic energy dissipation in the impeller are shown in Figure 19, where the streamlines in guide vane channels are also shown. Here $P_t = (-\overline{\rho u_i' u_j'}) \frac{\partial \overline{u_i}}{\partial x_j}$ indicates the turbulent kinetic energy production. The flow downstream the trailing edge of the blades corresponds to a high turbulent kinetic energy production since the flow near the pressure side and suction side of the blades, with different flow velocity, mix in this region. The P_t near the blade upstream the stalled guide vane channels is higher than the P_t near the blade upstream the unstalled guide vane channels. Figures 20 and 21 show the instantaneous distributions of P_t and streamline in guide vane channels on the symmetry plane at conditions III and IV, respectively. The P_t in the stalled guide vane channels is higher than in the unstalled channels. The regions between straight flows (with high flow velocity), and separated flows (with low flow velocity), correspond to high P_t. The strong velocity gradient in these regions may be responsible for the large P_t.

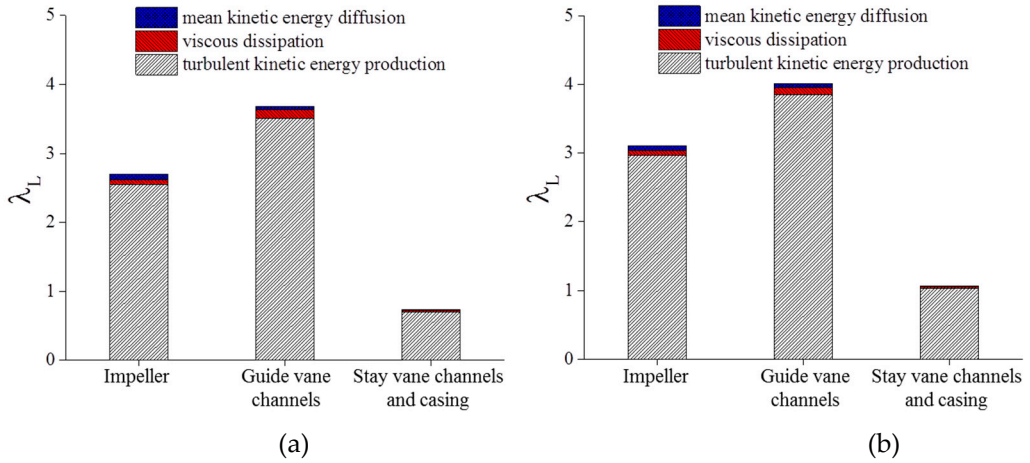

Figure 18. Composition of the loss coefficient at conditions (**a**) IV and (**b**) III.

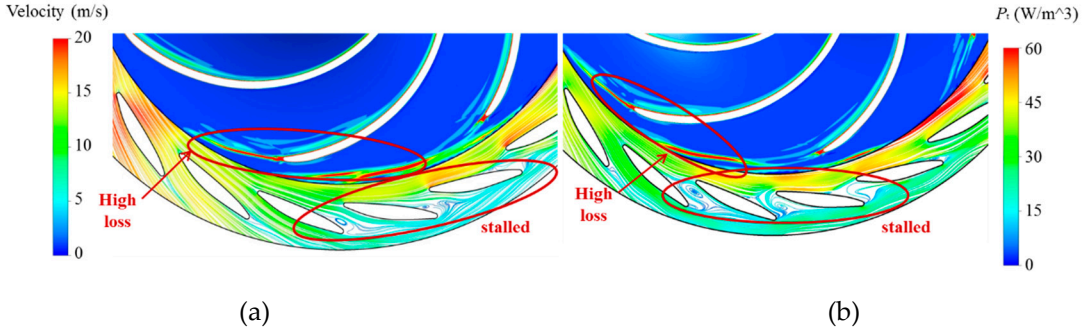

Figure 19. Instantaneous distributions of streamlines in guide vane channels and turbulent kinetic energy dissipation in the impeller at (**a**) condition IV and (**b**) III.

It was discussed in the previous section that there are several stalled guide vane channels at conditions III while the other several guide vane channels are stalling from condition III to IV. The P_t in these channels are higher than that in the other channels, which may be responsible for the sudden increase of the loss from condition III to IV, as shown in Figure 13.

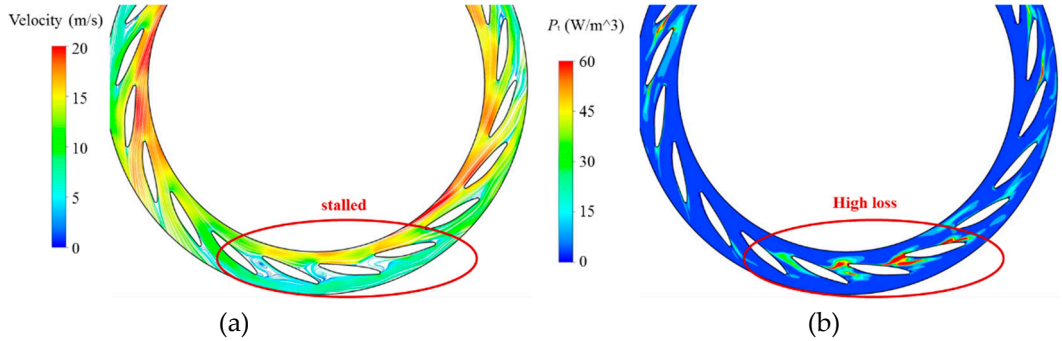

Figure 20. Instantaneous distributions of (**a**) streamlines and (**b**) turbulent kinetic energy dissipation in guide vane channels at condition III.

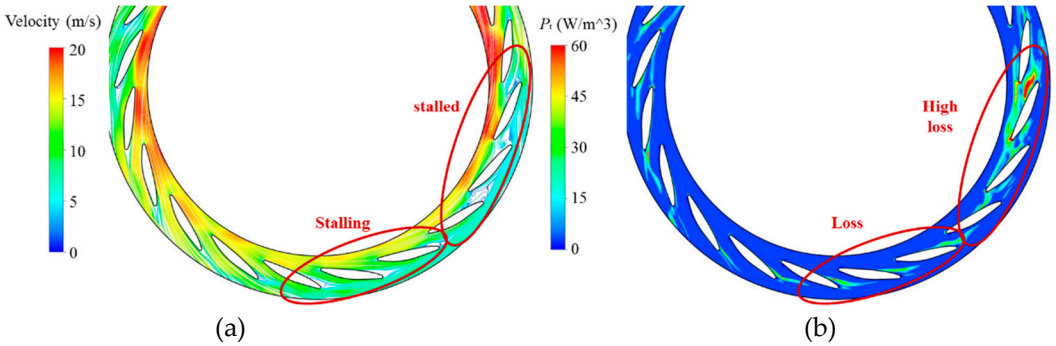

Figure 21. Instantaneous distributions of (**a**) streamlines and (**b**) turbulent kinetic energy dissipation in guide vane channels at condition IV.

5.2.2. Condition V

The analysis of the pressure fluctuations at condition V reveals the existence of rotating stall, suggesting that the flow pattern at this condition is highly time dependent, and that the contribution of the variation of the kinetic energy of the mean flow should be taken into account. Figure 22 illustrates the compositions of the loss coefficient at conditions V. The contribution of the variation of mean kinetic to the loss is insignificant so the conclusion is the same: most lost is converted to the turbulent kinetic energy.

The relationship between the flow patterns and the P_t distribution should be discussed at several time instances. Four various time instances are determined as shown in Figure 23. The instantaneous distributions of streamlines, pressure and P_t in guide vane channels at these time instances are illustrated in Figure 24. The occurrence of the flow separation in Channel 1 downstream the monitoring point $gv1$ is detected at time 'a', where the pressure at $gv1$ is increasing while $gv6$ is decreasing, suggesting that the flow in Channel 1 is stalling. A high-pressure region in the channel neighboring the fully stalled channel is detected. The region with high P_t is located between the straight flow and the separated flow. Then the flow in Channel 1 becomes fully stalled at time 'b' and the high-pressure region circumferentially moves to Channel 1. The P_t in the region with separated flow is still high, but lower than that at time 'a' since no straight flow exists in this channel. At time 'c', Channel 1 is recovering where the pressure at $gv1$ is decreasing while it is increasing at $gv6$. The existence of both straight flow and separated flow in Channel 1 at this time instance leads to a high P_t region. The flow

in Channel 1 recovers to straight flow at time 'd' and only a minor separated region near the trailing edge of the guide vane is detected.

The instantaneous distributions of streamlines, pressure and P_t in the impeller are illustrated in Figure 25. The existence of a rotating stall at condition V indicates that the flow pattern leading to the stalled guide vane channels moves circumferentially. The P_t near the blade upstream the stalled guide vane channels is always higher than that upstream the unstalled guide vane channels.

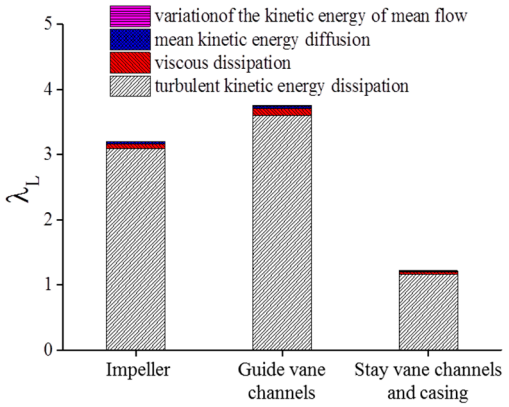

Figure 22. Composition of the loss coefficient at condition V.

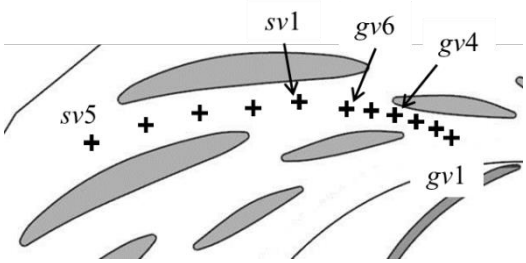

(a)

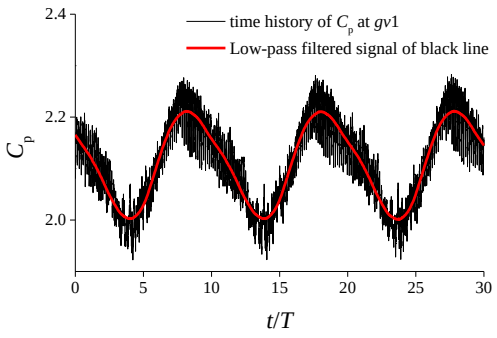

(b)

Figure 23. *Cont.*

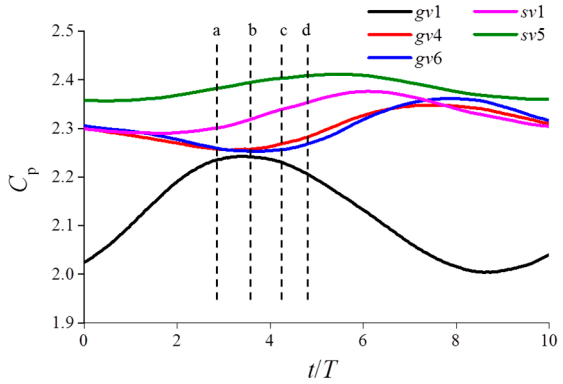

(c)

Figure 23. Pressure coefficient analysis. (**a**) Locations of monitoring points in the guide vane and stay vane channel, (**b**) time history of C_p at $gv1$ at condition V by black line while the red line is the low-pass filtered signal of black line as well as (**c**) low-pass filtered signal of C_p at these points and four time instances.

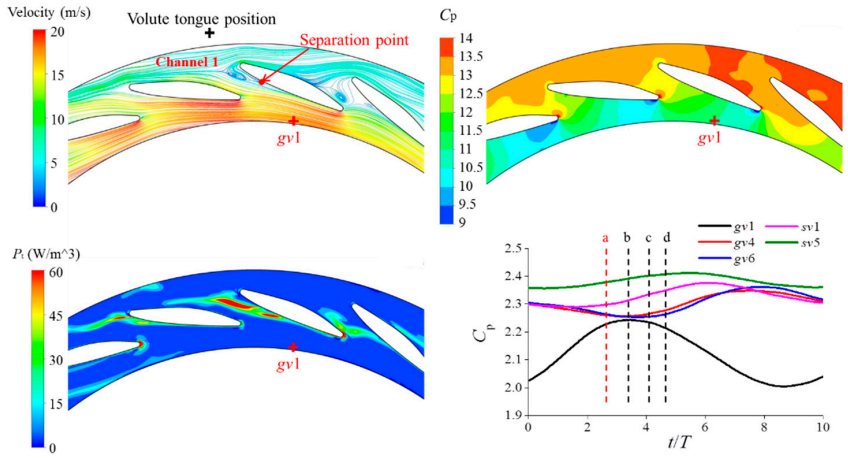

(a)

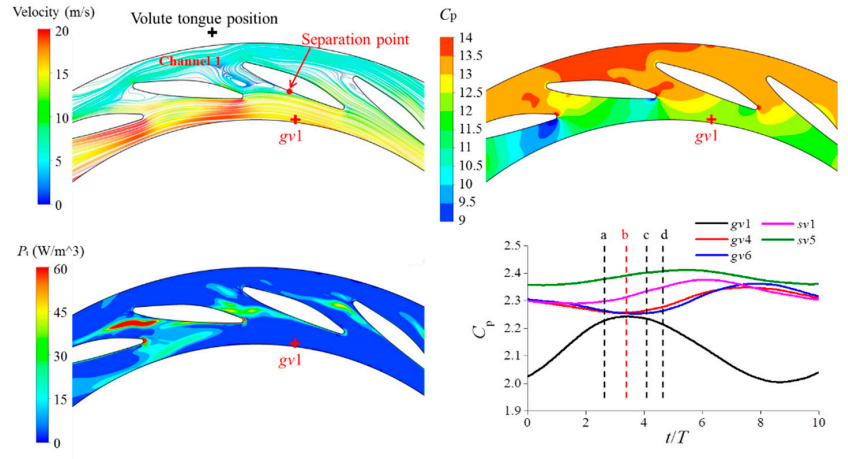

(b)

Figure 24. *Cont.*

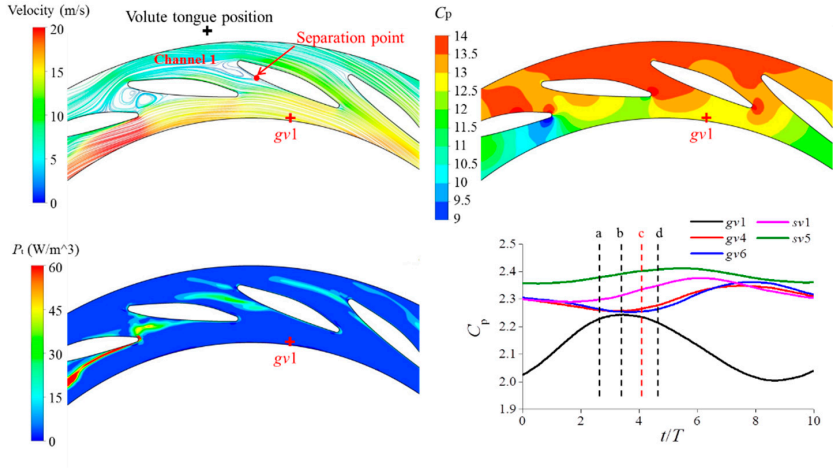

(c)

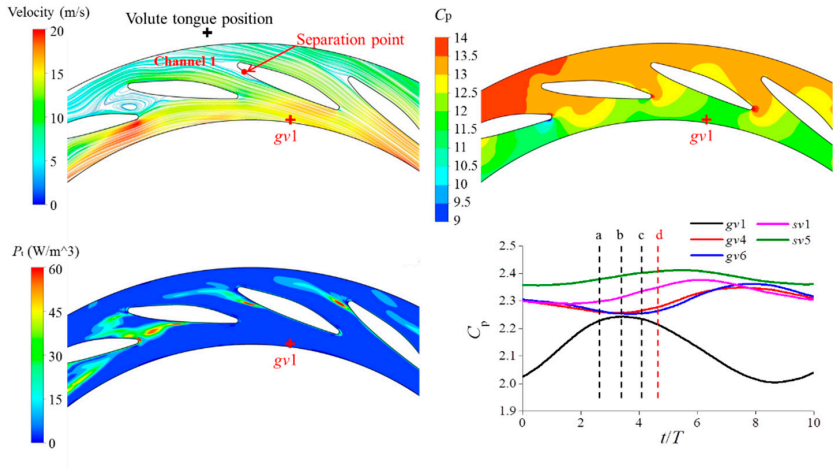

(d)

Figure 24. Instantaneous distributions of streamlines (left top), pressure (right top) and turbulent kinetic energy dissipation (left bottom) in guide vane channels at condition V. Subfigures (**a**–**d**) correspond to the conditions at related time instance.

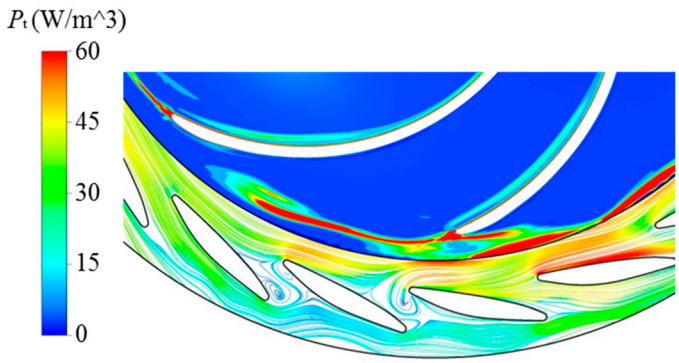

Figure 25. Instantaneous distributions of turbulent kinetic energy dissipation in the impeller and streamlines in guide vane channels at condition V.

6. Concluding Remarks

The mechanism of the positive slope on the pump performance curve in a low specific speed model pump-turbine was numerically investigated against experiments. Conclusions were drawn as follows:

1. According to the theoretical derivation, the occurrence of the positive slope on the pump performance curve corresponds to the region where $\frac{\partial P_u}{\partial Q}$ is larger than a critical value $\frac{P_u}{Q}$. The substantial decrease of λ_u results in the positive slope in the pump performance curve. For this decrease of λ_u in the present study, about 80% is attributed to the decrease of the input power coefficient while the remaining 20% is caused the increase of the loss coefficient.
2. The unsteady local loss analysis, derived from the energy equation, was conducted to illustrate the contribution of local flow patterns to the loss in corresponding hydraulic components. The variation of the kinetic energy of the mean flow was taken into account for the first time so that this method could be applied on highly time dependent flow patterns, including the rotating stall in the present study.
3. The local loss analysis reveals that, the majority of the loss converts to the turbulent kinetic energy in the pump-turbine. The regions between the straight flow with high flow velocity and the separated flow with low flow velocity have great contributions to the loss, due to the strong velocity gradient.
4. Some guide vane channels were stalled at the condition with larger discharge coefficient than the positive slope region. Then several guide vane channels near the stalled channels were stalling with minor decrease of the discharge coefficient, leading to sudden increases of the input power and the loss. When the discharge coefficient slightly decreased in further, the pump-turbine operated into the positive slope and the rotating stall with 3 stall cells appeared, proven by the FFT and cross-phase analysis on pressure fluctuations.

Author Contributions: Conceptualization, Z.Z. and S.L.; Methodology, G.L. and Z.Z.; Validation, G.L., D.L. and Z.Z.; Formal Analysis, G.L. and D.L.; Investigation, Z.Z. and S.L.; Data Curation, Z.Z. and D.L.; Writing-Original Draft Preparation, G.L., Z.Z. and S.L.; Writing-Review & Editing, G.L. and Z.Z.; Supervision, S.L. and Z.Z.; Project Administration, Z.Z. and S.L.; Funding Acquisition, Z.Z. and S.L.

Acknowledgments: This research was funded by National Key R&D Program of China (2018YFB0606101) and National Natural Science Foundation of China (No.51876100).

Conflicts of Interest: The authors declare that they have no conflict of interest.

References

1. Braun, O. Part Load Flow in Radial Centrifugal Pumps. Ph.D. Thesis, École Polytechnique Fédérale de Lausanne, Lausanne, Switzerland, 2009.
2. Mei, Z.Y. *Technology of Pumped Storage Power Generation*; China Machine Press: Beijing, China, 2000. (In Chinese)
3. Hasmatuchi, V. Hydrodynamics of a Pump-Turbine Operating at Off-Design Conditions in Generating Mode. Ph.D. Thesis, École Polytechnique Fédérale de Lausanne, Lausanne, Switzerland, 2012.
4. Zuo, Z.G.; Liu, S.H. Flow-Induced Instabilities in Pump-Turbines in China. *Engineering* **2017**, *3*, 504–511. [CrossRef]
5. Gülich, J.F. *Centrifugal Pumps*; Springer: Berlin, Germany, 2008.
6. Eisele, K.; Muggli, F.; Zhang, Z.; Casey, M.; Sallaberger, M. Experimental and numerical studies of flow instabilities in pump-turbine stages. In Proceedings of the XIX IAHR Symposium, Singapore, 9–11 September 1998.
7. Pacot, O. Large Scale Computation of the Rotating Stall in a Pump-Turbine Using an Overset Finite Element Large Eddy Simulation Numerical Code. Ph.D. Thesis, École Polytechnique Fédérale de Lausanne, Lausanne, Switzerland, 2014.

8. Ciocan, G.D.; Kueny, J.L. Experimental Analysis of Rotor Stator Interaction in a Pump-Turbine. In Proceedings of the XXIII IAHR Symposium on Hydraulic Machinery and Systems, Yokohama, Japan, 17–21 October 2006.
9. Braun, O.; Kueny, J.L.; Avellan, F. Numerical analysis of flow phenomena related to the unstable energy-discharge characteristic of a pump-turbine in pump mode. In Proceedings of the ASME 2005 Fluids Engineering Division Summer Meeting, Houston, TX, USA, 19–23 June 2005; American Society of Mechanical Engineers: New York, NY, USA, 2005.
10. Zuo, Z.G.; Fan, H.G.; Liu, S.H.; Wu, Y.L. S-shaped characteristics on the performance curves of pump-turbines in turbine mode—A review. *Renew. Sustain. Energy Rev.* **2016**, *60*, 836–851. [CrossRef]
11. Yang, J. Flow Patterns Causing Saddle Instability in the Performance Curve of a Centrifugal Pump with Vaned Diffuser. Ph.D. Thesis, Jiangsu Univeristy, Zhenjiang, China, 2014.
12. Liu, J.T.; Liu, S.H.; Sun, Y.K.; Jiao, L.; Wu, Y.L.; Wang, L.Q. Three-dimensional flow simulation of transient power interruption process of a prototype pump-turbine at pump mode. *J. Mech. Sci. Technol.* **2013**, *27*, 1305–1312. [CrossRef]
13. Sun, Y.K. Instability Characteristics and Influencing Factors of Positive Slope on Pump Performance Curves of A Low-Specific-Speed Pump-Turbine. Ph.D. Thesis, Tsinghua University, Beijing, China, 2016.
14. Ran, H.J. Study on Two Kinds of Unstable Characteristic Phenomena in Middle Specific Speed Pump Turbines. Ph.D. Thesis, Tsinghua University, Beijing, China, 2010.
15. Paik, J.; Fotis, S.; Sale, M. Numerical simulation of swirling flow in complex hydroturbine draft tube using unsteady statistical turbulence models. *J. Hydraul. Eng.* **2005**, *131*, 441–456. [CrossRef]
16. Gehrer, A.; Helmut, B.; Köstenberger, M. Unsteady simulation of the flow through a horizontal-shaft bulb turbine. In Proceedings of the 22nd IAHR Symposium on Hydraulic Maschines and Systems, Stockholm, Sweden, 29 June–2 July 2004.
17. Spalart, P.; Shur, M. On the sensitization of turbulence models to rotation and curvature. *Aerosp. Sci. Technol.* **1997**, *1*, 297–302. [CrossRef]
18. Lu, G.C.; Zuo, Z.G.; Sun, Y.K.; Liu, D.M.; Tsujimoto, Y.; Liu, S.H. Experimental evidence of cavitation influences on the positive slope on the pump performance curve of a low specific speed model pump-turbine. *Renew. Energy* **2017**, *13*, 1539–1550. [CrossRef]
19. Durbin, P.A. Separated Flow Computations with the k-ε-v2 Model. *AIAA J.* **1995**, *33*, 659–664. [CrossRef]
20. Behnia, M.; Parneix, S.; Shabany, Y.; Durbin, P.A. Numerical Study of Turbulent Heat Transfer in Confined and Unconfined Impinging Jets. *Int. J. Heat Fluid Flow* **1999**, *20*, 1–9. [CrossRef]
21. Zuo, Z.G.; Liu, S.H.; Sun, Y.K.; Wu, Y.L. Pressure fluctuations in the vaneless space of high-head pump-turbines—A review. *Renew. Sustain. Energy Rev.* **2015**, *41*, 965–974. [CrossRef]
22. Sun, Y.K.; Zuo, Z.G.; Liu, S.H.; Liu, J.T.; Wu, Y.L. Distribution of pressure fluctuations in a prototype pump turbine at pump mode. *Adv. Mech. Eng.* **2014**, *6*, 923937. [CrossRef]
23. Wilhelm, S.; Balarac, G.; Metais, O.; Segoufin, C. Analysis of head losses in a turbine draft tube by means of 3D unsteady simulations. *Flow Turbul. Combust.* **2016**, *97*, 1255–1280. [CrossRef]
24. Li, D.Y.; Gong, R.Z.; Wang, H.J.; Xiang, G.M.; Wei, X.Z.; Qin, D.Q. Entropy production analysis for hump characteristics of a pump turbine model. *Chin. J. Mech. Eng.* **2016**, *29*, 803–812. [CrossRef]
25. Erne, S.; Gernot, E.; Christian, B. Numerical Study of the Stay Vane Channel-Flow in a reversible Pump Turbine at Off-Design Conditions. In Proceedings of the 16th International Conference on Fluid Flow Technologies, Budapest, Hungary, 1–4 September 2015.